

Chiral Second-Harmonic Generation from Monolayer WS₂/Aluminum Plasmonic Vortex Metalens

Wan-Ping Guo, Wei-Yun Liang, Chang-Wei Cheng, Wei-Lin Wu, Yen-Ting Wang, Quan Sun, Shuai Zu, Hiroaki Misawa, Pi-Ju Cheng, Shu-Wei Chang, Hyeyoung Ahn,* Minn-Tsong Lin,* and Shangjir Gwo*



Cite This: *Nano Lett.* 2020, 20, 2857–2864



Read Online

ACCESS |

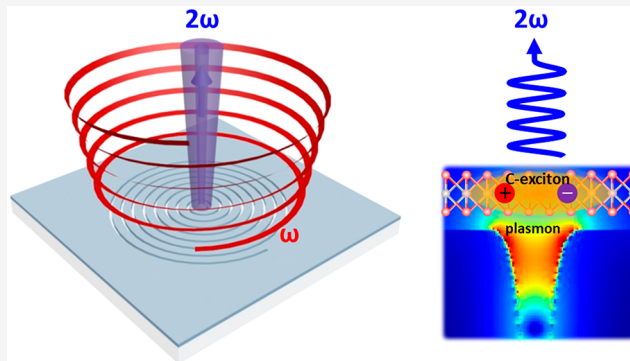
Metrics & More

Article Recommendations

Supporting Information

ABSTRACT: Two-dimensional spiral plasmonic structures have emerged as a versatile approach to generate near-field vortex fields with tunable topological charges. We demonstrate here a far-field approach to observe the chiral second-harmonic generation (SHG) at designated visible wavelengths from a single plasmonic vortex metalens. This metalens comprises an Archimedean spiral slit fabricated on atomically flat aluminum epitaxial film, which allows for precise tuning of plasmonic resonances and subsequent transfer of two-dimensional materials on top of the spiral slit. The nonlinear optical measurements show a giant SHG circular dichroism. Furthermore, we have achieved an enhanced chiral SHG conversion efficiency (about an order of magnitude greater than the bare aluminum lens) from monolayer tungsten disulfide (WS₂)/aluminum metalens, which is designed at the C-exciton resonance of WS₂. Since the C-exciton is not a valley exciton, the enhanced chiral SHG in this hybrid system originates from the plasmonic vortex field-enhanced SHG under the optical spin–orbit interaction.

KEYWORDS: Surface plasmonic vortex metalens, optical spin–orbit interaction, chiral nonlinearity, second-harmonic generation, aluminum epitaxial film, monolayer tungsten disulfide



Besides spin angular momentum (SAM) associated with circular polarization, a light beam can carry orbital angular momentum (OAM) in free space, which corresponds to an optical vortex beam along the propagation axis with a helical phase front.^{1–4} It is well-known that the value of SAM per photon is limited to $\pm\hbar$ (\hbar is the reduced Planck constant, $\hbar = h/2\pi$), depending on right- or left-handed circular polarization (RCP or LCP). In contrast to SAM, the azimuthal phase (φ) dependence in the optical vortex beam is $\exp(il\varphi)$, where l is the topological charge per photon (positive or negative integer) and the value of OAM per photon is $l\hbar$. In anisotropic and inhomogeneous optical media, these two momenta can interact with each other, changing both the polarization and phase of the beam.⁴ This interaction can be controlled by the polarization of incident beam and the geometry of media resulting from their inhomogeneity. In the past two decades, optical vortex beams have found numerous applications such as optical manipulation of microparticles,^{5,6} super-resolution focusing,⁷ nonlinear vortex optics,⁸ optical communication,⁹ quantum information processing,^{10–12} topological photonics using the geometric phases,^{13–15} and optical vortex beam microemitters.^{16,17}

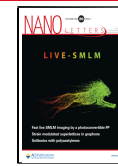
Optical vortex beams are typically generated in free space by diffraction-limited optical approaches.^{1–4} In the past decade or

so, surface plasmonic vortices generated by plasmonic nanostructures, such as Archimedean spiral nanoslits or nanogrooves fabricated on noble metal films,^{18–25} have attracted much interest because of the capability of plasmonic nanostructures to confine, manipulate, and enhance electromagnetic fields into subwavelength mode volumes.^{26–29} Therefore, plasmonic vortices formed through excitation of surface plasmon polaritons (SPPs) at the metal–dielectric interfaces by circularly polarized excitation beams can open a new pathway to dramatically shrink the vortex sizes,^{24,25} which could be exploited for integrated nanophotonic applications. However, to date, surface plasmonic vortices are mostly limited by investigations using near-field techniques, such as scanning near-field optical microscopy (SNOM),^{19–23} photoemission electron microscopy (PEEM),^{24,25} and scanning electron-beam-based cathodoluminescence (CL).³⁰ Therefore, it is highly desirable to generate far-field orbital angular momenta

Received: February 14, 2020

Revised: March 9, 2020

Published: March 12, 2020



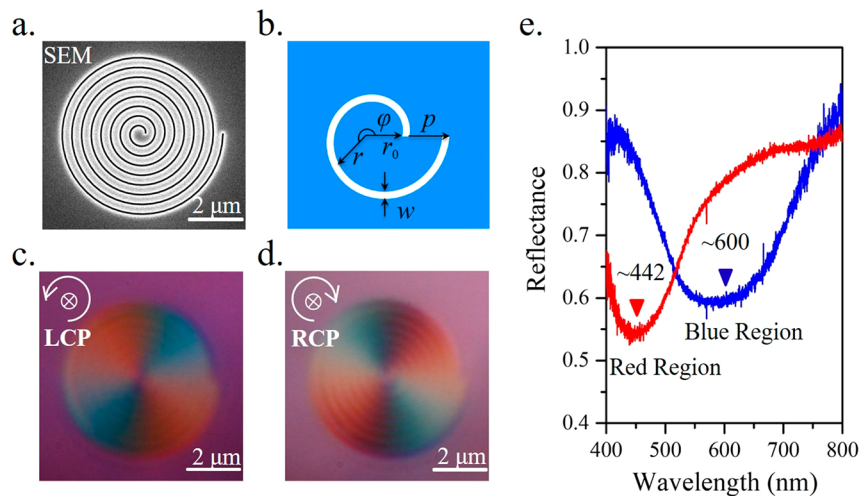


Figure 1. Geometric structure of the Archimedean plasmonic vortex lens and its optical response at far field. (a) Scanning electron microscopy (SEM) image of the plasmonic vortex lens, consisting of an 8-turn Archimedean nanoslit spiral ($r_0 = 200$ nm, $p = 370$ nm, $w = 140$ nm), which was milled through a 90 nm thick single-crystalline aluminum (111) epitaxial film grown on a sapphire (0001) substrate by focused-ion beam. (b) The definition of the Archimedean spiral is $r = r_0 + \varphi \cdot p / 2\pi$. (c,d) Optical microscopy images measured by LCP and RCP light at normal incidence. (e) Reflectance spectra of red and blue regions shown in (c,d). Two resonant absorption wavelengths at 442 and 600 nm originating from the nanoslit gap modes can be clearly observed in this structure.

from near-field optical chirality both for fundamental studies and applications.³¹

In this work, we combine plasmon-enhanced second-harmonic generation (SHG)^{32–35} with circular dichroism (CD) for probing the chirality of a plasmonic vortex metalens (PVML) consisting of an aluminum Archimedean spiral nanoslit and a semiconducting transition metal dichalcogenide (TMDC) monolayer. The advantage of SHG for probing near-field chirality is that the absorption cross section is not constrained by reciprocity,³⁶ and it can exhibit CD in planar chiral geometries and metasurfaces.^{37,38} As an optical medium, monolayer TMDC belongs to a class of layered materials, which can be readily exfoliated into monolayers due to weak van der Waals (vdW) interlayer bonding. Two-dimensional (2D) TMDCs show novel electronic and optical properties,³⁹ most notably the indirect-to-direct bandgap transition in the monolayer limit. Furthermore, the broken inversion symmetry in monolayer TMDCs can lead to strong nonlinear optical responses, such as SHG,^{40–42} and valley-selective circular dichroism in the emerging field of valleytronics.⁴³ Additional advantage for the hybrid-material metalens applications is that monolayer TMDCs can be easily integrated with dissimilar materials (semiconductors, dielectrics, and metals) via vdW bonding without the constraint of lattice matching condition in conventional semiconductor and metal heteroepitaxy.

The plasmonic spiral structures used here were fabricated on aluminum epitaxial films, which exhibit dual resonance bands (442 and 600 nm), where the 442 nm resonance is specifically designed to match with the C-exciton resonance in monolayer tungsten disulfide (WS₂) originating from “band nesting”.⁴⁴ Unlike the valley excitons, that is, A and B excitons associated with the interband transitions at the degenerate but inequivalent K and K' (i.e., K and -K) valleys of the Brillouin zone, the C-exciton resonance does not exhibit the intrinsic chiroptical properties of valley excitons.⁴³ Therefore, it is suitable for the demonstration of artificially engineered chirality using the plasmonic enhancement effects of PVML under the optical spin-orbit interaction. Furthermore, we can significantly enhance the SHG intensity, in comparison to the

bare aluminum lens, by incorporating a monolayer of WS₂ onto the lens.

In our PVML design, SPPs are excited at the Archimedean spiral slit edge at designated wavelengths (i.e., plasmonic gap modes) and propagate radially at the top (air/metal) and bottom (metal/substrate) interfaces (Figures S1 and S2). Moreover, a large-area exfoliated monolayer WS₂ is transferred to the Archimedean spiral slit by using a gold-mediated technique.⁴⁵ In Figure 1a, we show the actual Archimedean spiral slit fabricated by focused-ion beam (FIB) milling on an atomically flat aluminum (Al) film epitaxially grown on sapphire (root-mean-square film roughness: ~0.5 nm over a $5 \times 5 \mu\text{m}^2$ area).^{46,47} The advantages of Al are that it is an excellent plasmonic material at both visible and ultraviolet (UV) wavelengths (alternative to silver (Ag) in the visible and better than Ag in the UV) and Al is chemically stable due to the formation a uniform native aluminum oxide layer with a self-passivating capability. Moreover, Al epitaxial films are compatible with the complementary metal-oxide semiconductor (CMOS) fabrication processes.^{48–50} It is also important for this study that Al is an appropriate plasmonic material for optical nonlinear processes, as demonstrated by earlier works.^{51–53}

The simple formula $r(\varphi) = r_0 + \varphi \cdot p / 2\pi$ in the polar coordinate system, as shown in Figure 1b, is used to design the Archimedean spiral with the starting radius $r_0 = 200$ nm, the pitch $p = 370$ nm, and the cycle number $n = 8$. By using a single-crystalline and atomically smooth Al film, we can precisely engineer plasmonic gap modes by controlling the film thickness (90 nm) and the slit width ($w = 140$ nm). Indeed, the optical microscopy images measured under LCP and RCP illumination at normal incidence clearly show chiroptical behavior of resonant absorption bands (Figure 1c,d). By performing reflectance spectromicroscopy (Figure 1e, optical measurements setup is shown in Figure S3) and finite-difference time-domain (FDTD) simulations (Figure S2), we show that this aluminum spiral has dual resonances at 442 and 600 nm (free-space wavelength).

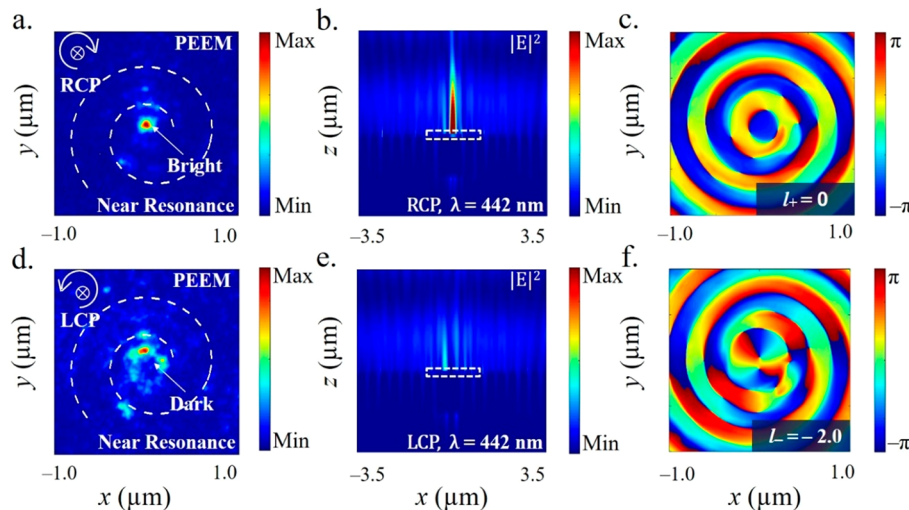


Figure 2. Photoemission electron microscopy (PEEM) measurement and finite-difference time-domain (FDTD) simulations for the chiral plasmonic modes at 442 nm. (a–c) PEEM image (field of view, 10 μm ; near resonance, 430 nm) and FDTD simulations of the plasmonic mode under RCP laser excitation. The electric field intensity simulated by FDTD at the cross-sectional x – z plane shows a focusing effect at the spiral core. (c) Phase image (E_z) simulated at the top interface near the center of spiral ($2 \times 2 \mu\text{m}^2$, x – y plane), which shows a topological charge l_+ of 0. (d–f) Results obtained by using LCP laser excitation. In the PEEM image, a dark region is found at the spiral core. The absence of the center focusing effect and a topological charge l_- of –2 can also be confirmed by FDTD simulations shown in (e,f).

According to the FDTD simulations, the 442 nm gap mode locates at the top (air/Al) interface, while the 600 nm gap mode is more complicated, involving both top and bottom (air/Al and Al/sapphire) interfaces. Therefore, in the following, we will focus more on the 442-mode because it is used to couple with the C-exciton resonance in monolayer WS₂ and detailed information about the 600 nm gap mode is included in the Supporting Information (Figures S2 and S4). In a simple modeling, the electric field of linear surface plasmonic vortex along the z -direction can be expressed by the following equation in the cylindrical coordinate set (r , φ , z)

$$E_{z,l}(\omega, r, \varphi) = E_0(\omega) \exp[i k_z(\omega) z] \exp[i l(\omega) \varphi] J_l[k_{\text{SPP}}(\omega) r] \quad (1)$$

where $k_0 = \frac{\omega}{c}$, $k_{\text{SPP}} = k_0 \sqrt{\frac{\epsilon_d \epsilon_m}{\epsilon_d + \epsilon_m}}$ (for the case of a thick metal film), and ω , c , ϵ_d , ϵ_m stand for the incident frequency, light vacuum velocity, and permittivity of dielectric and metal, respectively.^{18,19} The wavenumber perpendicular to the surface k_z , constrained by $k_{\text{SPP}}^2 + k_z^2 = k_0^2$, is purely imaginary ($k_{\text{SPP}} > k_0$, that is, $E_{z,l}$ is an evanescent field); and k_{SPP} is the radial wavenumber of SPP. Therefore, the properties of the surface evanescent field are determined by the l^{th} -order Bessel function of the first kind, $J_l[k_{\text{SPP}}(\omega)r]$ and the spiral phase profile of the SPP vortex field $\exp[i l(\omega) \varphi]$, where l is the topological charge. In the case of an ultrathin Al film, the SPP dispersion relation derived from the dielectric function is not directly applicable due to the strong near-field coupling between top- and bottom-interface plasmonic modes^{24,25} and we have to apply the FDTD technique to simulate the field distribution near the spiral surface, as shown in Figure 2b,c and e,f for the 442 nm incident light with RCP and LCP polarization, respectively. It is numerically confirmed for this specific Archimedean spiral that $\lambda_{\text{SPP}} = 370$ nm (i.e., spiral pitch = SPP wavelength) at the top interface when the incident wavelength is at 442 nm (Figure 2e,f).

The topological charge of frequency-dependent plasmonic vortex, that is, $l(\omega)$, comes from the contributions from both

geometrical phase (Φ_g) and dynamic phase (Φ_d). Among them, one full cycle of spiral leads to a 2π dynamic phase and the geometrical phase is $2m\pi$, where the geometrical topological charge m is defined by $m = p/\lambda_{\text{SPP}}$. The resonant plasmonic vortex condition is that the total phase $\Phi_{\text{total}} = \Phi_g + \Phi_d = 2n\pi(m + 1)$ for an n -cycle spiral must be an even number of π . Here, the spin quantum number (handedness) of the incident photon is defined with respect to the propagation direction of the incident beam and we denote σ_{\pm} for the SAM of RCP ($\sigma_+ = +1$) and LCP ($\sigma_- = -1$) incident beam, respectively. Using the same convention, the counterclockwise spiral shown in Figure 1a corresponds to a negative geometrical topological charge ($m < 0$). The topological charge $l(\omega)$ of plasmonic vortex is then the sum of the spin angular momentum (σ_{\pm}) and the incident-frequency-dependent geometrical topological charge $m(\omega)$, that is

$$l_{\pm}(\omega) = \sigma_{\pm} + m(\omega) \quad (2)$$

For the top-interface plasmonic vortex mode at 442 nm, $m = -1$ and then we have the following relation: $l_{\pm}(\omega) = \sigma_{\pm} - 1$. As a result, the SPP field distribution at the center of the spiral strongly depends on the handedness of the circular polarization state of incoming light. For the present (counterclockwise) spiral structure, it can focus the RCP illumination into a bright spot ($l = 0$) at the center of lens. On the other hand, under the LCP illumination a doughnut-shaped intensity distribution with a hollow center appears at the center ($l = -2$).^{19,21} Therefore, this spiral structure can function as a spin-number (i.e., chirality)-dependent plasmonic vortex lens.

These theoretical predictions are experimentally confirmed by PEEM measurements^{5,55} (Figure 2a,d) and FDTD simulations (Figure 2b,c and e,f). In order to verify the chirality effects of the plasmonic vortex lens, circular-polarization-dependent PEEM measurements were performed by a commercial PEEM system (ELMITEC GmbH), which is capable of a 4 nm spatial resolution, and the experimental results are shown in Figure 2a,d. To perform the PEEM measurements, the circular-polarized excitation source is from

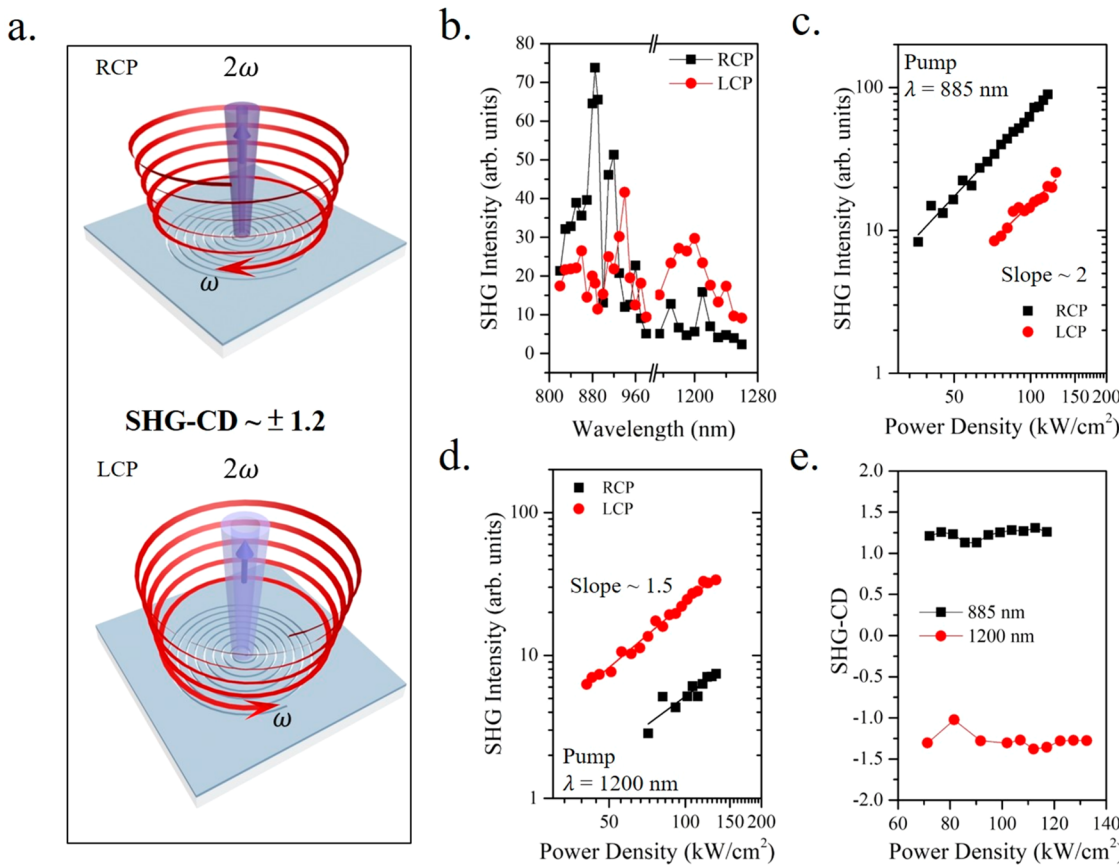


Figure 3. Second-harmonic (2ω) chiroptical spectra from the aluminum plasmonic vortex lens. (a) Schematic illustration of the measurement geometry. (b) Two distinct chiral SHG peaks appear at $\lambda_1 = 885$ nm and $\lambda_2 = 1200$ nm while scanning the fundamental wavelength of excitation laser (pulse width, 140 fs; repetition rate, 80 MHz) in the range of 820–1260 nm (820–980 nm and 1160–1260 nm), which are in agreement with the SPP resonance bands at 442 and 600 nm shown in Figure 1e. (c) At $\lambda_1 = 885$ nm, $\text{SHG}_{\text{RCP}} \gg \text{SHG}_{\text{LCP}}$ due to the plasmonic vortex lens effect and the SHG intensity follows the quadratic dependence on the average excitation power density (slope ~ 2 in the log–log plot). The peak power density can be estimated from the average power density by using the pulsed laser duty cycle. (d) By contrast, at $\lambda_2 = 1200$ nm, $\text{SHG}_{\text{RCP}} < \text{SHG}_{\text{LCP}}$ and the SHG intensity deviates from the quadratic dependence (slope ~ 1.5) in the log–log scale. (e) The measured SHG-CD, that is, $|I_{\text{RCP}}(2\omega) - I_{\text{LCP}}(2\omega)|/[I_{\text{RCP}}(2\omega) + I_{\text{LCP}}(2\omega))/2]$, is as high as ± 1.2 ($\pm 120\%$) for two chiral SPP bands.

a near-resonance ($\lambda = 430$ nm) laser beam produced by a mode-locked femtosecond Ti-sapphire laser (pulse duration: 100 fs, repetition rate: 77 MHz), frequency doubling with a beta barium borate (BBO) nonlinear crystal and passing through a quarter wave plate. In Figure 2b,c and e,f, the simulated electric-field distributions are in good agreement with the laser PEEM experimental results. The circular-polarization-dependent near-field linear responses illustrate that under the RCP excitation, a bright point appears at the center of spiral (Figure 2a); while under the LCP excitation, a dark circular region forms at the center of spiral (Figure 2d), indicating that a plasmonic vortex has been built up. As an experimental verification, the chiroptical reflection image obtained with the LCP illumination (Figure 1c) is also consistent with the expected field intensity from the azimuthal phase variation of the $l = -2$ mode at 442 nm. On the basis of these results, we clearly demonstrate that chirality effects can be observed using our vortex lens design.

Now, we turn our attention to the discussion of the main results: chirality-dependent SHG from a PVML at room temperature. Figure 3 shows the chiral SHG spectra from the bare aluminum plasmonic vortex lens (note that we could not collect any SHG signal from a flat aluminum film). Two distinct chiral SHG peaks ($\lambda_1 = 885$ and $\lambda_2 = 1200$ nm) with

strong dependence on the incident circular polarization states can be found while scanning the fundamental wavelength of excitation laser in the range of 820–1260 nm (more precisely, 820–980 nm and 1160–1260 nm). These results are in good agreement with the observed plasmonic resonance bands at 442 and 600 nm, as shown in Figure 1e. The chiral SHG response also exhibits a very sensitive dependence on the incident wavelength (Figure 3b), which can be expected from the superlinear dependence of SHG intensity, denoted as $I_{\text{RCP/LCP}}(2\omega)$, on the circularly polarized laser excitation power density. At $\lambda_1 = 885$ nm, the chirality-dependent SHG measurements indicate that the SHG intensity is stronger than that at $\lambda_2 = 1200$ nm and $\text{SHG}_{\text{RCP}} > \text{SHG}_{\text{LCP}}$ by a factor of about 4. Moreover, the SHG intensity shows a quadratic dependence (slope ~ 2 in the logarithmic plot) on the excitation power density (Figure 3c). By contrast, at $\lambda_2 = 1200$ nm, $\text{SHG}_{\text{RCP}} < \text{SHG}_{\text{LCP}}$ and the SHG intensity deviates from the quadratic dependence (slope ~ 1.5) due to a more complicated emission mechanism involving both top and bottom interfaces. In Supporting Information, we show the FDTD simulations of the near-field SHG intensity ($|E(2\omega)|^2$) distributions for both resonance modes (Figure S4e,f). The simulation results indicate that for the 885 nm excitation the SHG signals from both RCP and LCP incident light originate

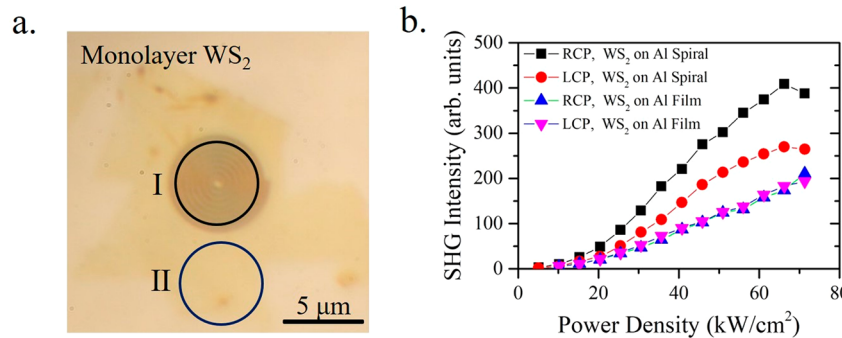


Figure 4. Excitation power density dependence of chiral SHG intensity from a single monolayer WS₂, including both regions coupled to the aluminum plasmonic vortex lens (region I, on the same lens structure shown in Figure 1a) and the uncoupled region (region II, bare aluminum film). (a) Optical image of monolayer WS₂ on an aluminum film patterned with an Archimedean plasmonic vortex lens structure. (b) Excitation power density dependence of the chiral SHG emission (C-exciton resonance at 442 nm) from monolayer WS₂ coupled to the aluminum plasmonic vortex lens (excitation laser is at $\lambda_1 = 885$ nm). On the bare aluminum region, the SHG intensity shows an achiral behavior due to the fact that the C-exciton is not a valley exciton, unlike the A and B excitons.

from the top interface (air/Al) and the observation of SHG_{RCP} > SHG_{LCP} can be attributed to the effects of plasmonic vortex lens (Figure 2). On the other hand, for the 1200 nm excitation the SHG signals from RCP and LCP incident light occurs at both top (air/Al) and bottom (Al/sapphire) interfaces, and the SHG signal is stronger at the bottom interface and SHG_{RCP} < SHG_{LCP} at the top interface. These simulation results are in good agreement with the experimental observation.

If we define that the SHG circular dichroism (SHG-CD) is equal to $|I_{RCP}(2\omega) - I_{LCP}(2\omega)| / [(I_{RCP}(2\omega) + I_{LCP}(2\omega)) / 2]$,^{37,38} we can quantitatively evaluate the plasmonic vortex lens performance for both RCP- and LCP-excitation to be as high as ± 1.2 (i.e., 120%, see Figure 3e), which is much higher than the reported values for 2D chiral plasmonic nanostructures (Table S1) in the literature. The nonlinear power conversion efficiency (CE), defined as CE = $P_{2\omega}/P_\omega$, is another important figure of merit for SHG. For our metalens structure, under an average power density of ~ 26 kW/cm² at $\lambda_1 = 885$ nm, we obtain CEs of 6.7×10^{-9} and 1.8×10^{-9} at RCP and LCP excitation, respectively, which are comparable to the SHG-CEs obtained for a gold Archimedean spiral lens.³²

To further enhance the SHG-CE, we incorporate a WS₂ monolayer onto the aluminum spiral lens because the broken inversion symmetry in monolayer TMDC can lead to a strong SHG response.^{40–42} For monolayer TMDCs, the conduction band minimum and the valence band maximum are both located at the K/K' corners of the hexagonal Brillouin zone. The A and B excitons associated with K/K' valley show a unique exciton-enhanced SHG process, following two-photon optical selection rules. It has been reported that two RCP photons at the fundamental frequency can generate a single LCP photon at the second-harmonic frequency with near-unity polarization, and vice versa.⁴⁰ Therefore, we adopt the C-exciton absorption at ~ 442 nm (Figure S5) for the demonstration of artificially engineered chirality effect because the C-exciton does not have intrinsic chiral properties, such as the A and B valley excitons.⁴⁴

In Figure 4, a large-area monolayer WS₂ is transferred to the sample surface, covering both the region aluminum plasmonic vortex lens (region I) and bare aluminum film (region II). The plasmonic vortex lens show an enhancement of SHG about 2.5 (RCP) and 1.5 (LCP) times stronger, compared to the monolayer WS₂ region on the base aluminum film (Figure S6). More importantly, we have demonstrated that the C-exciton in

WS₂ can exhibit an artificially engineered SHG chirality at room temperature on the plasmonic vortex lens (Figure 4b) and the SHG-CD is ~ 0.40 ($I_{RCP}/I_{LCP} \approx 1.5$). In comparison with the bare aluminum spiral, the SHG-CEs have been enhanced to 4.26×10^{-8} (6.4 times larger) and 2.74×10^{-8} (15.2 times larger) for RCP and LCP laser excitation, respectively (the detailed CE values are listed in Table S2).

In summary, we have developed a CMOS-compatible epitaxial plasmonic system (aluminum on sapphire), which is used for large-scale fabrication and integration of planar chiral plasmonic structures and 2D van der Waals materials. Specifically, we have achieved an enhanced chiral SHG conversion efficiency from a monolayer WS₂/aluminum vortex metalens (about an order of magnitude greater than that of a bare aluminum vortex lens), where the plasmonic vortex field is at the achiral C-exciton resonance (2ω). We have experimentally confirmed that using circularly polarized (RCP and LCP) laser excitation (ω), the chiral SHG from the bare aluminum vortex lens at the C-exciton resonance shows a strong circular dichroism due to the incident-light chirality effects of the plasmonic vortex, such that the observed chiral ratio (I_{RCP}/I_{LCP}) ≈ 4 and SHG-CD $\approx 120\%$. In the case of an exfoliated monolayer WS₂ resonantly coupled to the plasmonic vortex, we show that the chiral SHG at the C-exciton resonance can exhibit an artificially engineered chiral ratio $I_{RCP}/I_{LCP} \approx 1.5$ and SHG-CD $\approx 40\%$.

The hybrid material approach reported here, 2D materials in combination with chiral plasmonic structures on epitaxial aluminum films, has the potential to controllably integrate individual chiral hybrid-material systems into large-scale quantum architectures. These chiral quantum architectures can find important applications in chiral quantum optics,⁵⁶ as well as chiral coupling of excitons and light through plasmon-exciton coupling^{57,58} and optical spin-orbit interactions.^{59,60}

■ ASSOCIATED CONTENT

SI Supporting Information

The Supporting Information is available free of charge at <https://pubs.acs.org/doi/10.1021/acs.nanolett.0c00645>.

Experimental methods; details about the sample structure (Figure S1) and the plasmonic gap modes (additional FDTD simulations, Figures S2 and S4); linear and nonlinear optical measurement setups (Figure S3); SHG from an exfoliated monolayer WS₂ on SiO₂/Si

at around the C-exciton resonance (Figure S5); circular polarization-dependent SHG enhancement factors from an exfoliated monolayer WS₂ (Figure S6); literature results of linear and nonlinear circular dichroism effects from 2D metal nanostructures (Table S1); circular polarization-dependent SHG-CD and conversion efficiencies of monolayer WS₂ with and without the plasmonic vortex lens (Table S2) (PDF)

AUTHOR INFORMATION

Corresponding Authors

Hyeyoung Ahn — Department of Photonics, College of Electrical and Computer Engineering, National Chiao-Tung University, Hsinchu 30010, Taiwan;  orcid.org/0000-0003-3209-6724; Email: hyahn@mail.nctu.edu.tw

Minn-Tsong Lin — Department of Physics, National Taiwan University, Taipei 10617, Taiwan; Research Center for Applied Sciences, Academia Sinica, Taipei 11529, Taiwan; Email: mtlin@phys.ntu.edu.tw

Shangjr Gwo — Department of Physics, National Tsing-Hua University, Hsinchu 30013, Taiwan; Research Center for Applied Sciences, Academia Sinica, Taipei 11529, Taiwan; Department of Electrophysics, National Chiao-Tung University, Hsinchu 30010, Taiwan;  orcid.org/0000-0002-3013-0477; Email: gwo@phys.nthu.edu.tw

Authors

Wan-Ping Guo — Department of Physics, National Taiwan University, Taipei 10617, Taiwan

Wei-Yun Liang — Department of Photonics, College of Electrical and Computer Engineering, National Chiao-Tung University, Hsinchu 30010, Taiwan

Chang-Wei Cheng — Department of Physics, National Tsing-Hua University, Hsinchu 30013, Taiwan

Wei-Lin Wu — Department of Physics, National Tsing-Hua University, Hsinchu 30013, Taiwan

Yen-Ting Wang — Department of Electrophysics, National Chiao-Tung University, Hsinchu 30010, Taiwan

Quan Sun — Research Institute for Electronic Science, Hokkaido University, Sapporo 001-0021, Japan;  orcid.org/0000-0001-5413-8038

Shuai Zu — Research Institute for Electronic Science, Hokkaido University, Sapporo 001-0021, Japan

Hiroaki Misawa — Research Institute for Electronic Science, Hokkaido University, Sapporo 001-0021, Japan; Center for Emergent Functional Matter Science, National Chiao-Tung University, Hsinchu 30010, Taiwan;  orcid.org/0000-0003-1070-387X

Pi-Ju Cheng — Research Center for Applied Sciences, Academia Sinica, Taipei 11529, Taiwan

Shu-Wei Chang — Research Center for Applied Sciences, Academia Sinica, Taipei 11529, Taiwan

Complete contact information is available at:

<https://pubs.acs.org/10.1021/acs.nanolett.0c00645>

Notes

The authors declare no competing financial interest.

ACKNOWLEDGMENTS

S.G., H.A., M.-T.L. would like to acknowledge the funding support from the Ministry of Science and Technology in Taiwan for this research work (Grants: MOST 108-2119-M-

007-008, MOST 107-2923-M-007-004-MY3, MOST 107-2119-M-002-006, MOST 107-2112-M-009-015-MY3, and MOST 107-2923-M-009-003-MY3). H.M. acknowledges the support by JSPS KAKENHI (Grant JP18H05205), the support from the Nanotechnology Platform (Hokkaido University), and Dynamic Alliance for Open Innovation Bridging Human, Environment, and Materials (Five-Star Alliance) of MEXT.

REFERENCES

- (1) Allen, L.; Beijersbergen, M. W.; Spreeuw, R. J. C.; Woerdman, J. P. Orbital angular momentum of light and the transformation of Laguerre-Gaussian laser modes. *Phys. Rev. A: At., Mol., Opt. Phys.* **1992**, *45*, 8185–8189.
- (2) Padgett, M.; Courtial, J.; Allen, L. Light's orbital angular momentum. *Phys. Today* **2004**, *57* (5), 35–40.
- (3) Yao, A. M.; Padgett, M. J. Orbital angular momentum: origins, behavior and applications. *Adv. Opt. Photonics* **2011**, *3*, 161–204.
- (4) Marrucci, L.; Manzo, C.; Paparo, D. Optical spin-to-orbital angular momentum conversion in inhomogeneous anisotropic media. *Phys. Rev. Lett.* **2006**, *96*, 163905.
- (5) Padgett, M.; Bowman, R. Tweezers with a twist. *Nat. Photonics* **2011**, *5*, 343–348.
- (6) Tsai, W.-Y.; Huang, J.-S.; Huang, C.-B. Selective trapping or rotation of isotropic dielectric microparticles by optical near field in a plasmonic Archimedes spiral. *Nano Lett.* **2014**, *14*, 547–552.
- (7) David, A.; Gjonaj, B.; Blau, Y.; Dolev, S.; Bartal, G. Nanoscale shaping and focusing of visible light in planar metal-oxide-silicon waveguides. *Optica* **2015**, *2*, 1045–1048.
- (8) Dorney, K. M.; Rego, L.; Brooks, N. J.; San Román, J.; Liao, C.-T.; Ellis, J. L.; Zusin, D.; Gentry, C.; Nguyen, Q. L.; Shaw, J. M.; Picón, A.; Plaja, L.; Kapteyn, H. C.; Murnane, M. M.; Hernández-García, C. Controlling the polarization and vortex charge of attosecond high-harmonic beams via simultaneous spin-orbit momentum conservation. *Nat. Photonics* **2019**, *13*, 123–130.
- (9) Bozinovic, N.; Yue, Y.; Ren, Y.; Tur, M.; Kristensen, P.; Huang, H.; Willner, A. E.; Ramachandran, S. Terabit-scale orbital angular momentum mode division multiplexing in fibers. *Science* **2013**, *340*, 1545–1548.
- (10) Mair, A.; Vaziri, A.; Weihs, G.; Zeilinger, A. Entanglement of the orbital angular momentum states of photons. *Nature* **2001**, *412*, 313–316.
- (11) Nicolas, A.; Veissier, L.; Giner, L.; Giacobino, E.; Maxein, D.; Laurat, J. A quantum memory for orbital angular momentum photonic qubits. *Nat. Photonics* **2014**, *8*, 234–238.
- (12) Chen, L.; Lei, J.; Romero, J. Quantum digital spiral imaging. *Light: Sci. Appl.* **2014**, *3*, No. e153.
- (13) Berry, M. V. Optical vortices evolving from helicoidal integer and fractional phase steps. *J. Opt. A: Pure Appl. Opt.* **2004**, *6*, 259–268.
- (14) Marrucci, L.; Manzo, C.; Paparo, D. Pancharatnam–Berry phase optical elements for wave front shaping in the visible domain: Switchable helical mode generation. *Appl. Phys. Lett.* **2006**, *88*, 221102.
- (15) Cohen, E.; Larocque, H.; Bouchard, F.; Nejadsattari, F.; Gefen, Y.; Karimi, E. Geometric phase from Aharonov–Bohm to Pancharatnam–Berry and beyond. *Nat. Rev. Phys.* **2019**, *1*, 437–449.
- (16) Cai, X.; Wang, J.; Strain, M. J.; Johnson-Morris, B.; Zhu, J.; Sorel, M.; O'Brien, J. L.; Thompson, M. G.; Yu, S. Integrated compact optical vortex beam emitters. *Science* **2012**, *338*, 363–366.
- (17) Miao, P.; Zhang, Z.; Sun, J.; Walasik, W.; Longhi, S.; Litchinitser, N. M.; Feng, L. Orbital angular momentum microlaser. *Science* **2016**, *353*, 464–467.
- (18) Ohno, T.; Miyaniishi, S. Study of surface plasmon chirality induced by Archimedes' spiral grooves. *Opt. Express* **2006**, *14*, 6285–6290.
- (19) Gorodetski, Y.; Niv, A.; Kleiner, V.; Hasman, E. Observation of the spin-based plasmonic effect in nanoscale structures. *Phys. Rev. Lett.* **2008**, *101*, 043903.

- (20) Kim, H.; Park, J.; Cho, S.-W.; Lee, S.-Y.; Kang, M.; Lee, B. Synthesis and dynamic switching of surface plasmon vortices with plasmonic vortex lens. *Nano Lett.* **2010**, *10*, 529–536.
- (21) Chen, W.; Abeysinghe, D. C.; Nelson, R. L.; Zhan, Q. Experimental confirmation of miniature spiral plasmonic lens as a circular polarization analyzer. *Nano Lett.* **2010**, *10*, 2075–2079.
- (22) Chen, C.-F.; Ku, C.-T.; Tai, Y.-H.; Wei, P.-K.; Lin, H.-N.; Huang, C.-B. Creating optical near-field orbital angular momentum in a gold metasurface. *Nano Lett.* **2015**, *15*, 2746–2750.
- (23) David, A.; Gjonaj, B.; Bartal, G. Two-dimensional optical nanovortices at visible light. *Phys. Rev. B: Condens. Matter Mater. Phys.* **2016**, *93*, No. 121302.
- (24) Spektor, G.; Kilbane, D.; Mahro, A. K.; Frank, B.; Ristok, S.; Gal, L.; Kahl, P.; Podbiel, D.; Mathias, S.; Giessen, H.; Meyer zu Heringdorf, F.-J.; Orenstein, M.; Aeschlimann, M. Revealing the subfemtosecond dynamics of orbital angular momentum in nano-plasmonic vortices. *Science* **2017**, *355*, 1187–1191.
- (25) Frank, B.; Kahl, P.; Podbiel, D.; Spektor, G.; Orenstein, M.; Fu, L.; Weiss, T.; Horn-von Hoegen, M.; Davis, T. J.; Meyer zu Heringdorf, F.-J.; Giessen, H. Short-range surface plasmonics: localized electron emission dynamics from a 60-nm spot on an atomically flat single-crystalline gold surface. *Sci. Adv.* **2017**, *3*, No. e1700721.
- (26) Barnes, W. L.; Dereux, A.; Ebbesen, T. W. Surface plasmon subwavelength optics. *Nature* **2003**, *424*, 824–830.
- (27) Stockman, M. I. Nanofocusing of optical energy in tapered plasmonic waveguides. *Phys. Rev. Lett.* **2004**, *93*, 137404.
- (28) Schuller, J. A.; Barnard, E. S.; Cai, W.; Jun, Y. C.; White, J. S.; Brongersma, M. L. Plasmonics for extreme light concentration and manipulation. *Nat. Mater.* **2010**, *9*, 193–204.
- (29) Atwater, H. A.; Polman, A. Plasmonics for improved photovoltaic devices. *Nat. Mater.* **2010**, *9*, 205–213.
- (30) Hachtel, J. A.; Cho, S.-Y.; Davidson, R. B.; Feldman, M. A.; Chisholm, M. F.; Haglund, R. F.; Idrobo, J. C.; Pantelides, S. T.; Lawrie, B. J. Spatially and spectrally resolved orbital angular momentum interactions in plasmonic vortex generators. *Light: Sci. Appl.* **2019**, *8*, 33.
- (31) Gorodetski, Y.; Drezen, A.; Genet, C.; Ebbesen, T. W. Generating far-field orbital angular momenta from near-field optical chirality. *Phys. Rev. Lett.* **2013**, *110*, 203906.
- (32) Davidson, R. B., II; Ziegler, J. I.; Vargas, G.; Avanesyan, S. M.; Gong, Y.; Hess, W.; Haglund, R. F. Efficient forward second-harmonic generation from planar Archimedean nanospirals. *Nanophotonics* **2015**, *4*, 108–113.
- (33) Butet, J.; Brevet, P.-F.; Martin, O. J. F. Optical second harmonic generation in plasmonic nanostructures: from fundamental principles to advanced applications. *ACS Nano* **2015**, *9*, 10545–10562.
- (34) Wang, C.-Y.; Chen, H.-Y.; Sun, L.; Chen, W.-L.; Chang, Y.-M.; Ahn, H.; Li, X.; Gwo, S. Giant colloidal silver crystals for low-loss linear and nonlinear plasmonics. *Nat. Commun.* **2015**, *6*, 7734.
- (35) Gwo, S.; Wang, C.-Y.; Chen, H.-Y.; Lin, M.-H.; Sun, L.; Li, X.; Chen, W.-L.; Chang, Y.-M.; Ahn, H. Plasmonic metasurfaces for nonlinear optics and quantitative SERS. *ACS Photonics* **2016**, *3*, 1371–1384.
- (36) Hopkins, B.; Poddubny, A. N.; Miroshnichenko, A. E.; Kivshar, Y. S. Circular dichroism induced by Fano resonances in planar chiral oligomers. *Laser Photonics Rev.* **2016**, *10*, 137–146.
- (37) Valev, V. K.; Baumberg, J. J.; Sibilia, C.; Verbiest, T. Chirality and chiroptical effects in plasmonic nanostructures: Fundamentals, recent progress, and outlook. *Adv. Mater.* **2013**, *25*, 2517–2534.
- (38) Rodrigues, S. P.; Lan, S.; Kang, L.; Cui, Y.; Cai, W. Nonlinear imaging and spectroscopy of chiral metamaterials. *Adv. Mater.* **2014**, *26*, 6157–6162.
- (39) Mak, K. F.; Shan, J. Photonics and optoelectronics of 2D semiconductor transition metal dichalcogenides. *Nat. Photonics* **2016**, *10*, 216–226.
- (40) Seyler, K. L.; Schaibley, J. R.; Gong, P.; Rivera, P.; Jones, A. M.; Wu, S.; Yan, J.; Mandrus, D. G.; Yao, W.; Xu, X. Electrical control of second-harmonic generation in a WSe₂ monolayer transistor. *Nat. Nanotechnol.* **2015**, *10*, 407–411.
- (41) Wang, Z.; Dong, Z.; Zhu, H.; Jin, L.; Chiu, M.-H.; Li, L.-J.; Xu, Q.-H.; Eda, G.; Maier, S. A.; Wee, A. T. S.; Qiu, C.-W.; Yang, J. K. W. Selectively plasmon-enhanced second-harmonic generation from monolayer tungsten diselenide on flexible substrates. *ACS Nano* **2018**, *12*, 1859–1867.
- (42) Shi, J.; Liang, W.-Y.; Raja, S. S.; Sang, Y.; Zhang, X.-Q.; Chen, C.-A.; Wang, Y.; Yang, X.; Lee, Y.-H.; Ahn, H.; Gwo, S. Plasmonic enhancement and manipulation of optical nonlinearity in monolayer tungsten disulfide. *Laser Photonics Rev.* **2018**, *12*, 1800188.
- (43) Schaibley, J. R.; Yu, H.; Clark, G.; Rivera, P.; Ross, J. S.; Seyler, K. L.; Yao, W.; Xu, X. Valleytronics in 2D materials. *Nat. Rev. Mater.* **2016**, *1*, 16055.
- (44) Carvalho, A.; Ribeiro, R. M.; Castro Neto, A. H. Band nesting and the optical response of two-dimensional semiconducting transition metal dichalcogenides. *Phys. Rev. B: Condens. Matter Mater. Phys.* **2013**, *88*, 115205.
- (45) Desai, S. B.; Madhvapathy, S. R.; Amani, M.; Kiriya, D.; Hettick, M.; Tosun, M.; Zhou, Y.; Dubey, M.; Ager, J. W., III; Chrzan, D.; Javey, A. Gold-mediated exfoliation of ultralarge optoelectronically-perfect monolayers. *Adv. Mater.* **2016**, *28*, 4053–4058.
- (46) Cheng, F.; Su, P.-H.; Choi, J.; Gwo, S.; Li, X.; Shih, C.-K. Epitaxial Growth of atomically smooth aluminum on silicon and its intrinsic optical properties. *ACS Nano* **2016**, *10*, 9852–9860.
- (47) Cheng, C.-W.; Liao, Y.-J.; Liu, C.-Y.; Wu, B.-H.; Raja, S. S.; Wang, C.-Y.; Li, X.; Shih, C.-K.; Chen, L.-J.; Gwo, S. Epitaxial aluminum-on-sapphire films as a plasmonic material platform for ultraviolet and full visible spectral regions. *ACS Photonics* **2018**, *5*, 2624–2630.
- (48) Knight, M. W.; King, N. S.; Liu, L.; Everitt, H. O.; Nordlander, P.; Halas, N. J. Aluminum for plasmonics. *ACS Nano* **2014**, *8*, 834–840.
- (49) Zheng, B. Y.; Wang, Y.; Nordlander, P.; Halas, N. J. Color-selective and CMOS-compatible photodetection based on aluminum plasmonics. *Adv. Mater.* **2014**, *26*, 6318–6323.
- (50) Gwo, S.; Chen, H.-Y.; Lin, M.-H.; Sun, L.; Li, X. Nanomanipulation and controlled self-assembly of metal nanoparticles and nanocrystals for plasmonics. *Chem. Soc. Rev.* **2016**, *45*, 5672–5716.
- (51) Krause, D.; Teplin, C. W.; Rogers, C. T. Optical surface second harmonic measurements of isotropic thin-film metals: Gold, silver, copper, aluminum, and tantalum. *J. Appl. Phys.* **2004**, *96*, 3626–3634.
- (52) Castro-Lopez, M.; Brinks, D.; Sapienza, R.; van Hulst, N. F. Aluminum for nonlinear plasmonics: Resonance-driven polarized luminescence of Al, Ag, and Au nanoantennas. *Nano Lett.* **2011**, *11*, 4674–4678.
- (53) Yang, K.-Y.; Butet, J.; Yan, C.; Bernasconi, G. D.; Martin, O. J. F. Enhancement mechanisms of the second harmonic generation from double resonant aluminum nanostructures. *ACS Photonics* **2017**, *4*, 1522–1530.
- (54) Sun, Q.; Ueno, K.; Yu, H.; Kubo, A.; Matsuo, Y.; Misawa, H. Direct imaging of the near field and dynamics of surface plasmon resonance on gold nanostructures using photoemission electron microscopy. *Light: Sci. Appl.* **2013**, *2*, No. e118.
- (55) Razinskas, G.; Kilbane, D.; Melchior, P.; Geisler, P.; Krauss, E.; Mathias, S.; Hecht, B.; Aeschlimann, M. Normal-incidence PEEM imaging of propagating modes in a plasmonic nanocircuit. *Nano Lett.* **2016**, *16*, 6832–6837.
- (56) Lodahl, P.; Mahmoodian, S.; Stobbe, S.; Rauschenbeutel, A.; Schneeweiss, P.; Volz, J.; Pichler, H.; Zoller, P. Chiral quantum optics. *Nature* **2017**, *541*, 473–480.
- (57) Shi, J.; Lin, M.-H.; Chen, I.-T.; Mohammadi Estakhri, N.; Zhang, X.-Q.; Wang, Y.; Chen, H.-Y.; Chen, C.-A.; Shih, C.-K.; Alù, A.; Li, X.; Lee, Y.-H.; Gwo, S. Cascaded exciton energy transfer in a monolayer semiconductor lateral heterostructure assisted by surface plasmon polariton. *Nat. Commun.* **2017**, *8*, 35.
- (58) Sun, L.; Wang, C.-Y.; Krasnok, A.; Choi, J.; Shi, J.; Gomez Diaz, J. S.; Zepeda, A.; Gwo, S.; Shih, C.-K.; Alù, A.; Li, X. Separation of

valley excitons in a MoS₂ monolayer using a subwavelength asymmetric groove array. *Nat. Photonics* **2019**, *13*, 180–184.

(59) Gong, S.-H.; Alpeggiani, F.; Sciacca, B.; Garnett, E. C.; Kuipers, L. Nanoscale chiral valley-photon interface through optical spin-orbit coupling. *Science* **2018**, *359*, 443–447.

(60) Chen, P.; Lo, T. W.; Fan, Y.; Wang, S.; Huang, H.; Lei, D. Chiral coupling of valley excitons and light through photonic spin-orbit interactions. *Adv. Opt. Mater.* **2020**, *8*, 1901233.